

University of Nebraska - Lincoln

DigitalCommons@University of Nebraska - Lincoln

Faculty Publications, Department of Physics
and Astronomy

Research Papers in Physics and Astronomy

10-25-2019

Two-dimensional spin-valley locking spin valve

L. L. Tao

Evgeny Y. Tsymbal

Follow this and additional works at: <https://digitalcommons.unl.edu/physicsfacpub>



Part of the [Physics Commons](#)

This Article is brought to you for free and open access by the Research Papers in Physics and Astronomy at DigitalCommons@University of Nebraska - Lincoln. It has been accepted for inclusion in Faculty Publications, Department of Physics and Astronomy by an authorized administrator of DigitalCommons@University of Nebraska - Lincoln.

Two-dimensional spin-valley locking spin valveL. L. Tao^{*} and Evgeny Y. Tsymbal[†]*Department of Physics and Astronomy and Nebraska Center for Materials and Nanoscience,
University of Nebraska, Lincoln, Nebraska 68588, USA*

(Received 3 July 2019; published 25 October 2019)

Valleytronics is an emerging field of research which employs energy valleys in the band structure of two-dimensional (2D) electronic materials to encode information. A special interest has been triggered by the associated spin-valley coupling which reveals rich fundamental physics and enables new functionalities. Here, we propose exploiting the spin-valley locking in 2D materials with a large spin-orbit coupling and electric-field reversible valley spin polarization, such as germanene, stanene, a $1T'$ transition metal dichalcogenide (TMDC) monolayer, and a $2H$ -TMDC bilayer, to realize a valley spin valve (VSV). The valley spin polarization in these materials can be switched by an external electric field, which enables functionalities of a valley spin polarizer or a valley spin analyzer. When placed in series, they constitute the proposed VSV—a device whose conductance state is ON or OFF depending on the relative valley spin polarization of the polarizer and the analyzer. Using quantum-transport calculations based on an adequate tight-binding model, we predict a giant VSV ratio of nearly 100% for both germanene- and stanene-based VSV devices. Our results demonstrate the implication of the spin-valley coupling in 2D materials for the novel device concept promising for valleytronics.

DOI: [10.1103/PhysRevB.100.161110](https://doi.org/10.1103/PhysRevB.100.161110)

An electronic band structure of numerous crystalline materials exhibits inequivalent and well-separated energy extrema in the momentum space, known as valleys. The valley index (also known as valley pseudospin) represents a discrete degree of freedom for low-energy carriers, which can be used as a state variable to encode information. The exploitation and manipulation of the valley pseudospin manifests an emerging field of research dubbed valleytronics [1,2].

One of the central concepts of valleytronics is the valley polarization. In analogy to the spin polarization in spintronics [3], the valley polarization is a disbalance in the electron occupation of two valleys. Monolayer (ML) transition metal dichalcogenides MX_2 ($M = \text{Mo}, \text{W}; X = \text{S}, \text{Se}, \text{Te}$) [4] provide a promising platform to explore the rich valley physics, such as the valley selective circular dichroism [5,6], the valley Hall effect [7], and valley excitons [8]. Interesting phenomena and new functionalities are envisioned due to spin-valley coupling in these [9,10] and related [11] two-dimensional (2D) materials. In particular, the strong spin-valley coupling was shown to enhance the spin and valley polarization lifetime [1], lead to valley-controlled spin-dependent properties [9], and even produce magnetoelectric effects [12]. The spin-valley coupling allows control of the valley polarization by lifting the valley degeneracy. This can be achieved by applying an external magnetic field [13,14], by doping with transition metal atoms [15,16], or by growing on a magnetic insulator substrate via the proximity effect [17–21].

The valley pseudospin provides interesting opportunities for novel electronic devices. For example, in analogy to the spin-valve effect in magnetic tunnel junctions [22,23], a

valley-valve effect can be realized, which is the change of electrical resistance between two values modulated by the valley-dependent conductance. Since the intervalley transport requires flipping the valley index, the electric current is expected to be largely suppressed, which yields the high-resistance state. In contrast, the intravalley transport supports relatively low electrical resistance. The valley-valve effect has been predicted for a graphene nanoribbon where the valley polarization was inverted by local application of a gate voltage to the constriction region [24]. Related valley-valve effects in graphene were predicted, resulting from locally modulated electrostatic potentials [25,26].

In this work, we propose a valley spin valve (VSV), which relies on spin-valley locking. We consider a 2D system which has space-inversion (P) and time-reversal (T) symmetries and the band dispersion with two well-separated valleys K and K' related by T symmetry, where K is a non-time-reversal-invariant momentum (non-TRIM). In the absence of external electric field E , the band structure is both spin degenerate and valley degenerate [Fig. 1(a), central panel]. Application of electric field E breaks the P symmetry and splits the band structure into two spin subbands, in the presence of spin-orbit coupling (SOC) [Fig. 1(a), right panel]. Independent of the specific type of SOC [27], this spin splitting is Zeeman-like (i.e., the spin bands are split as if they were subject to an external magnetic field), resulting from the broken P symmetry and non-TRIM $K(K')$ valley point [9,28–30]. The spin polarizations are opposite between the two valleys as enforced by T symmetry. Changing the sign of E is equivalent to the P -symmetry operation, under which the momentum K transforms to $K'(-K)$ while the spin remains invariant. The valley-dependent spin polarization is therefore fully reversed [Fig. 1(a), left panel]. The switchable valley spin polarization can be realized in 2D materials, such as silicene [31,32],

^{*}Itao2@unl.edu[†]tsymbal@unl.edu

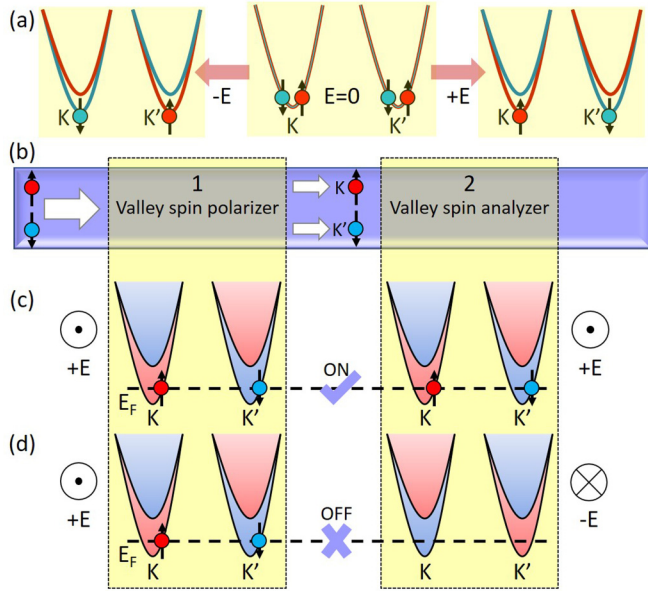


FIG. 1. (a) Schematic illustration of switchable valley spin polarization by applied electrical field E . K and K' denote two valleys, which are related by T symmetry. Arrows indicate spin states. (b) Schematic illustration of the valley spin valve for parallel (c) and antiparallel (d) applied electric fields in regions 1 (spin-valley polarizer) and 2 (spin-valley analyzer). The dashed line indicates the Fermi energy, E_F . Electrons (filled circles) can be transmitted (ON state) or blocked (OFF state) depending on the relative orientation of the electric field E in regions 1 and 2.

germanene [33], stanene [34,35], $1T'-MX_2$ ML [36], and $2H-MX_2$ bilayer (BL) [28]. All these materials have the required properties for the electric-field reversible valley spin polarization: they (i) preserve P and T symmetries, (ii) have well-separated valleys related by T symmetry and located at non-TRIM, and (iii) exhibit large SOC.

The electrically controlled effect of spin-valley locking is the key property of the proposed VSV. The working principle for the VSV is illustrated in Figs. 1(b), 1(c), and 1(d). Figure 1(b) shows schematics of the device structure where two regions, designated as 1 and 2, serve as a valley spin polarizer and a valley spin analyzer, respectively. The incoming electrons are neither spin polarized, nor valley polarized. In region 1, an electric field is applied normal to the plane. This field breaks the inversion symmetry and locks the spin and valley around the band edges so that electrons are spin-up polarized in valley K and spin-down polarized in valley K' [Fig. 1(b), left panels]. Thus, after being transmitted across the valley spin polarizer [region 1 in Fig. 1(b)], electrons become fully spin polarized in each valley, with the spin polarization having opposite sign in valleys K and K' . The valley spin analyzer [region 2 in Fig. 1(b)] selects electrons according to their valley spin polarization, which can be controlled by the direction of an applied electric field in this region. If the applied field in region 2 is parallel to that in region 1, the valley spin polarization of the analyzer is the same as that of the polarizer, as shown in Fig. 1(c), and both spin-up and spin-down electrons can be efficiently transmitted through the intravalley transport. This configuration is expected to have low resistance (ON state).

However, if the applied field in region 2 is antiparallel to that in region 1, the valley spin polarization of the analyzer is opposite to that of the polarizer, as shown in Fig. 1(d), and either-spin electrons encounter a potential barrier for the intravalley transport. Thus, this configuration is expected to produce much higher resistance of the device (OFF state).

To demonstrate the feasibility of the proposed VSV for realistic materials, we perform theoretical modeling of the electronic transport in germanene- and stanene-based devices, where SOC is expected to be sizable [37–39]. The tight-binding Hamiltonian for germanene or stanene is given by [38,40–42]

$$H = -t \sum_{\langle i,j \rangle \alpha} c_{i\alpha}^\dagger c_{j\alpha} + i \frac{\lambda_{SO}}{3\sqrt{3}} \sum_{\langle\langle i,j \rangle\rangle \alpha, \beta} v_{ij} c_{i\alpha}^\dagger \sigma_z^{\alpha\beta} c_{j\beta} + l E_z \sum_{i\alpha} \xi_i c_{i\alpha}^\dagger c_{i\alpha}, \quad (1)$$

where the first term is the nearest-neighbor hopping, $c_{i\alpha}^\dagger$ ($c_{j\alpha}$) is an electron creation (annihilation) operator at site i (j) with spin $\alpha = \uparrow, \downarrow$, t is the hopping parameter, and $\langle i, j \rangle$ denotes the sum over the nearest-neighbor sites. The second term represents the intrinsic SOC with strength λ_{SO} , $\langle\langle i, j \rangle\rangle$ denotes the sum over the next-nearest-neighbor sites, σ_z is the z component of the Pauli matrix, and $v_{ij} = +1$ (-1) selects anticlockwise (clockwise) hopping with respect to the z axis [Fig. 2(c)]. The third term arises from the applied electric field E_z , $\xi_i = +1$ (-1) distinguishes site $i = A(B)$, and l is the buckling height [Fig. 2(b)]. According to Eq. (1), $[\sigma_z, H] = 0$, and thus the spin component σ_z is a good quantum number. We note that within our model, we ignore both the electric-field-induced and intrinsic Rashba SOC. While the former is significantly smaller than the intrinsic SOC, the latter has a negligible effect on the calculated conductance (Supplemental Material Sec. 8 [43]). The following tight-binding parameters [37] are used for germanene: $t = 1.3$ eV, $\lambda_{SO} = 0.043$ eV, and $l = 0.33$ Å, and for stanene [38]: $t = 1.3$ eV, $\lambda_{SO} = 0.1$ eV, and $l = 0.4$ Å.

Figure 2(a) schematically shows the VSV structure, where the source (drain) electrode extends to $-\infty(+\infty)$ along the x direction and two gates are placed within the central region. The polarity of each gate is controlled independently. When the gate voltages have the same magnitude and sign, we define the device state as “parallel.” When the gate voltages have the same magnitude but opposite sign, we define the device state as “antiparallel.” The figure of merit characterizing the VSV effect is the VSV conductance ratio η , which is defined as $\eta = (G_P - G_{AP}) / (G_P + G_{AP})$, with G_P (G_{AP}) being the total conductance for the device in the parallel (antiparallel) state. Figure 2(d) shows the unit cell and the first Brillouin zone used for the band structure calculations.

We first investigate the electronic band structure of stanene tunable by electric field E_z , using the Hamiltonian model of Eq. (1). The results are shown in Fig. 3. For $E_z = 0$ [Fig. 3(a)], a band gap of 0.2 eV is opened at the K and K' points by SOC. As expected, the bands are spin degenerate due to the combination of inversion and time-reversal symmetries. When E_z is nonzero [$E_z = 1.25$ V/nm in Fig. 3(b) and $E_z = -1.25$ V/nm in Fig. 3(c)], the spin degeneracy is lifted due to inversion symmetry being broken, and the band gap is

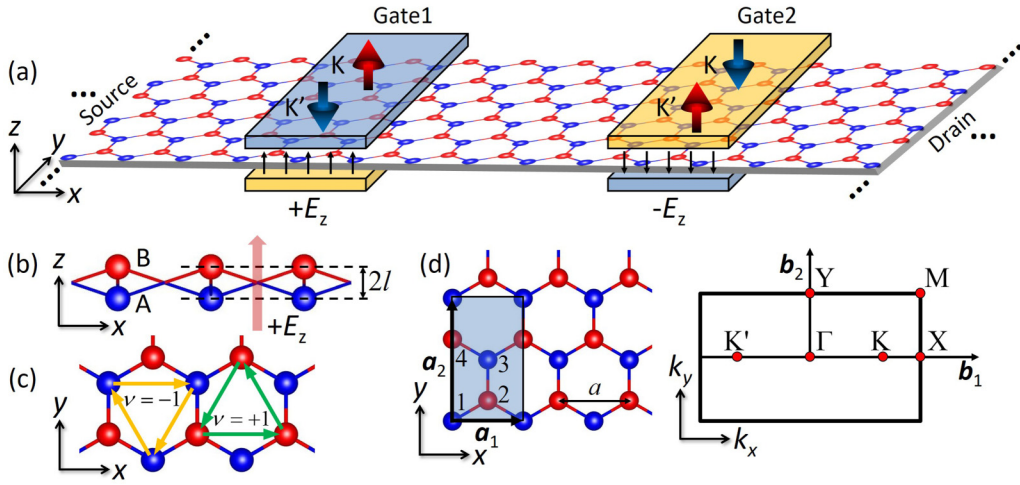


FIG. 2. (a) Schematic illustration of a two-terminal device model. The two gates of width d_1 are separated by distance d_2 . E_z (black solid arrows) is the electric field generated by the gate voltage. The red and blue arrows denote spin orientation in the K and K' valleys for each gated region. (b) Side view of the monolayer structure. $2l$ is the A - B sublattice buckling height. (c) Next-nearest-neighbor hopping for SOC. (d) Unit cell (left) and the first Brillouin zone (right) with high-symmetry k directions indicated, where $\mathbf{a}_1 = a\hat{x}$, $\mathbf{a}_2 = \sqrt{3}a\hat{y}$, $\mathbf{b}_1 = 2\pi/a\hat{x}$, $\mathbf{b}_2 = 2\pi/(\sqrt{3}a)\hat{y}$ and a is the lattice constant. Coordinates of the high-symmetry k points are $\Gamma(0, 0)$, $K(1/3, 0)$, $K'(-1/3, 0)$, $X(0.5, 0)$, $M(0.5, 0.5)$, $Y(0.0, 0.5)$.

reduced to 0.1 eV. The bulk band gap E_g is given by $E_g = 2|\tau\sigma_z\lambda_{SO} - lE_z|$ [38,44], where $\tau = \pm 1$ denotes the valley index K or K' . At the critical field $E_{cr} = \lambda_{SO}/l = 2.5$ V/nm, the band gap closes, as confirmed by Supplemental Material Fig. S1(b) [43]. Importantly, at finite E_z , the band structure is fully spin polarized around the bottom (top) of the conduction (valence) band for each valley (K or K'). Comparing Fig. 3(b) to Fig. 3(c) reveals that the reversal of E_z from positive to negative switches the spin polarization within each valley. This is due to the reversed staggered potential on the two stanene sublattices.

It is seen from the insets of Figs. 3(b) and 3(c) that, for the spin-up channel, the K valley eigenstate is mainly contributed by the orbitals on sites 1 and 3 [A sublattice in Fig. 2(d)], whereas the K' valley eigenstate is dominated by the orbitals on sites 2 and 4 [B sublattice in Fig. 2(d)]. Switching E_z

interchanges the roles of A and B sublattices, which in turn interchanges the K and K' valleys. This is consistent with the symmetry enforcement. Switching E_z is equivalent to space-inversion transformation, under which the wave vector K becomes $K'(-K)$ while spin remains invariant. The electronic structure of germanene (not shown) demonstrates qualitatively similar behavior.

Next, we explore the VSV effect using quantum-transport calculations for the device model shown in Fig. 2(a). The theoretical formalism for conductance and scattering state calculations is given in Supplemental Material Sec. 1 [43]. Figure 4(a) shows the calculated conductance versus the Fermi energy E_F for parallel (G_P) and antiparallel (G_{AP}) states of the VSV and the resulting VSV conductance ratio η for a stanene-based device. It is evident that when E_F is close to the conduction band minimum (CBM) E_c , the G_P is about four

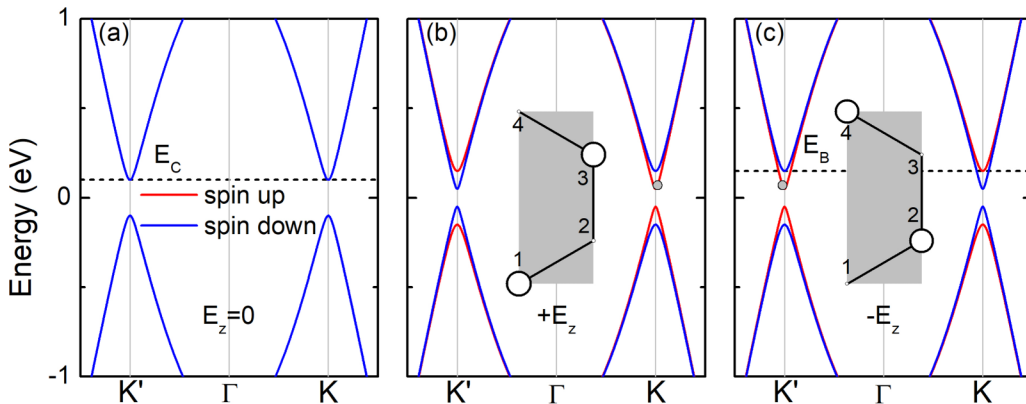


FIG. 3. Band structure of stanene along the X - Γ - X direction at the K and K' valleys for $E_z = 0$ (a), $E_z > 0$ ($E_z = 1.25$ V/nm) (b), and $E_z < 0$ ($E_z = -1.25$ V/nm) (c). The band structure along other k paths is shown in Fig. S1(a) of the Supplemental Material [43]. Insets in (b) and (c) show site-projected eigenstates $|\psi_1|^2$ at the energies near the CBM (indicated by filled gray circles). The site-projected weight is proportional to the radius of the open circle. E_c denotes the CBM for $E_z = 0$. E_B denotes the spin-up (spin-down) CBM at the K (K') point.

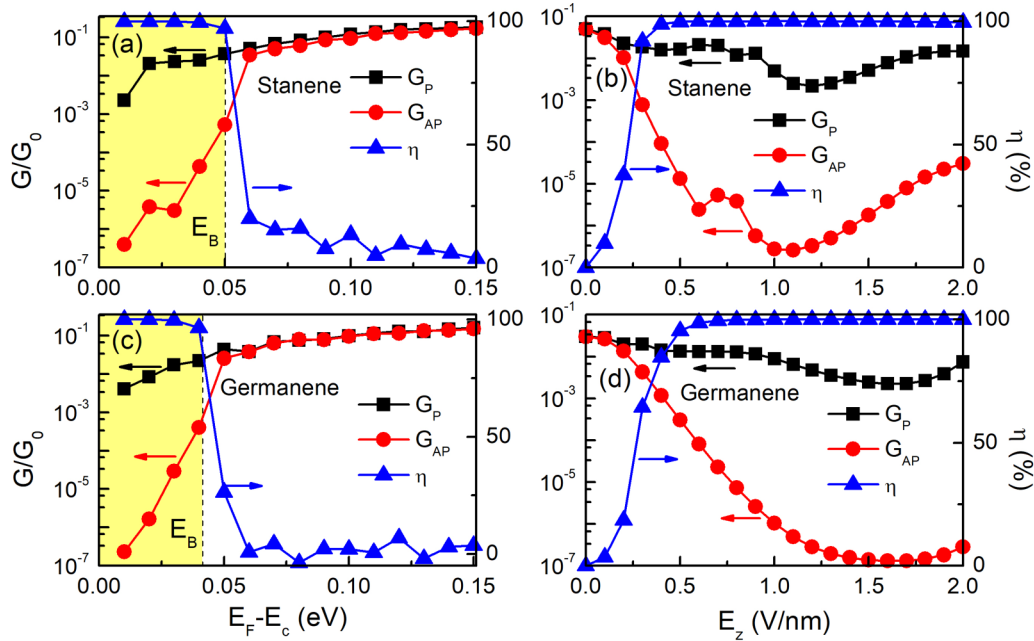


FIG. 4. Calculated conductance (G_P and G_{AP}) in units of $G_0 = 2e^2/h$ (left axis) and VSV conductance ratio η (right axis) as a function of the Fermi energy E_F for $|E_z| = 1.25$ V/nm (a),(c) and electric field E_z for $E_F = 0.01$ eV (b),(d) for stanene (a),(b) and germanene (c),(d), assuming $d_1 = 100a$ and $d_2 = 20a$. The vertical dashed lines denote the energy E_B indicated in Fig. 3(c). The yellow regions in (a) and (c) denote the energy window for achieving a giant VSV effect.

orders of magnitude larger than G_{AP} and η is nearly 100%. Such a giant VSV effect is sustained in the whole region of $E_F < E_B$ [highlighted in yellow in Fig. 4(a)], where E_B is the spin-up (spin-down) CBM at the K (K') valley [Fig. 3(c)]. This is due to the fact that in this region the valley spin analyzer [region 2 in Fig. 1(b)] is antiparallel aligned to the valley spin polarizer [region 1 in Fig. 1(b)] producing a potential barrier for either-spin electrons. When $E_F > E_B$ the incident energy becomes larger than the barrier height, resulting in an increase of G_{AP} and a decrease of η . We note that the energy window to achieve the giant VSV effect [the yellow region in Fig. 4(a)] is determined by the staggered potential, i.e., $E_F < |E_z|$.

Figure 4(b) shows the calculated conductance, G_P and G_{AP} , and the resulting VSV conductance ratio η as a function of E_z for $E_F = 0.01$ eV. It is seen that at small E_z , G_{AP} sharply decreases with the field E_z due to the formation of a potential barrier for electron transport in both valleys. This leads to an increase in VSV conductance ratio η which saturates at about 100% when the field reaches the value of $E_z = 0.4$ V/nm. A qualitatively similar behavior is observed for a germanene-based VSV, as shown in Figs. 4(c) and 4(d). We note that for observing a giant VSV effect, the gate width d_1 is required to be sufficiently large. On the contrary, for the ballistic transport considered in this work, the gate separation distance d_2 is not essential, as seen from Supplemental Material Fig. S2 [43].

The proposed working principle of the VSV has general importance and can be applied to other 2D materials provided that they have the inversion symmetry, well-separated valleys related by T symmetry and located at non-TRIM, and large SOC. In this regard, $1T'-MX_2$ ML [36] and $2H-MX_2$ BL [28] could also be suitable candidates for the electrically switchable spin polarization and the VSV realization. To illustrate their switchable behavior, we perform first-principles

calculations based on density functional theory (DFT), as described in Supplemental Material Sec. 2 [43].

Figures 5(a)–5(c) show the calculated electronic structure of a $1T'$ -MoS₂ monolayer around the K and K' points. Similar to germanene and stanene, in the absence of electric field, the band structure exhibits two spin-degenerate valleys [Fig. 5(a)]. Application of electric field E_z splits the bands into two spin subbands with opposite spin polarization at the two valleys K and K' [Fig. 5(b)]. Importantly, the polarity of the valley-dependent spin polarization is reversed by changing the direction of the electric field [Fig. 5(c)].

A similar behavior is observed for a $2H$ -MoS₂ bilayer, as seen from Figs. 5(d)–5(f). The spin degeneracy of the two-valley band structure is lifted by an applied electric field with spin polarization being opposite at the two valleys and being reversed with reversal of the electric field. It is noteworthy that the electric-field induced spin polarization has also been reported for a $2H$ -WSe₂ BL [28]. A further discussion regarding the physical origin for the switchable valley spin polarization can be found in Supplemental Material Secs. 6 and 7 [43]. We conclude therefore that $1T'-MX_2$ ML and $2H-MX_2$ BL represent other promising candidates to design a VSV, in addition to germanene and stanene.

Regarding the experimental realization of the VSV concept, germanene [25], stanene [26], $1T'-MX_2$ ML [45], and $2H-MX_2$ BL [28] have been successfully synthesized. The double-gate technique has been widely employed in 2D material based devices [46,47]. According to our calculations, electric fields in the order of 1 V/nm are required to achieve the desired performance of the VSV. These fields are readily attainable experimentally across a dielectric gate layer placed on a ML material [48]. We also find that the predicted effect is robust with respect to disorder which is always present in

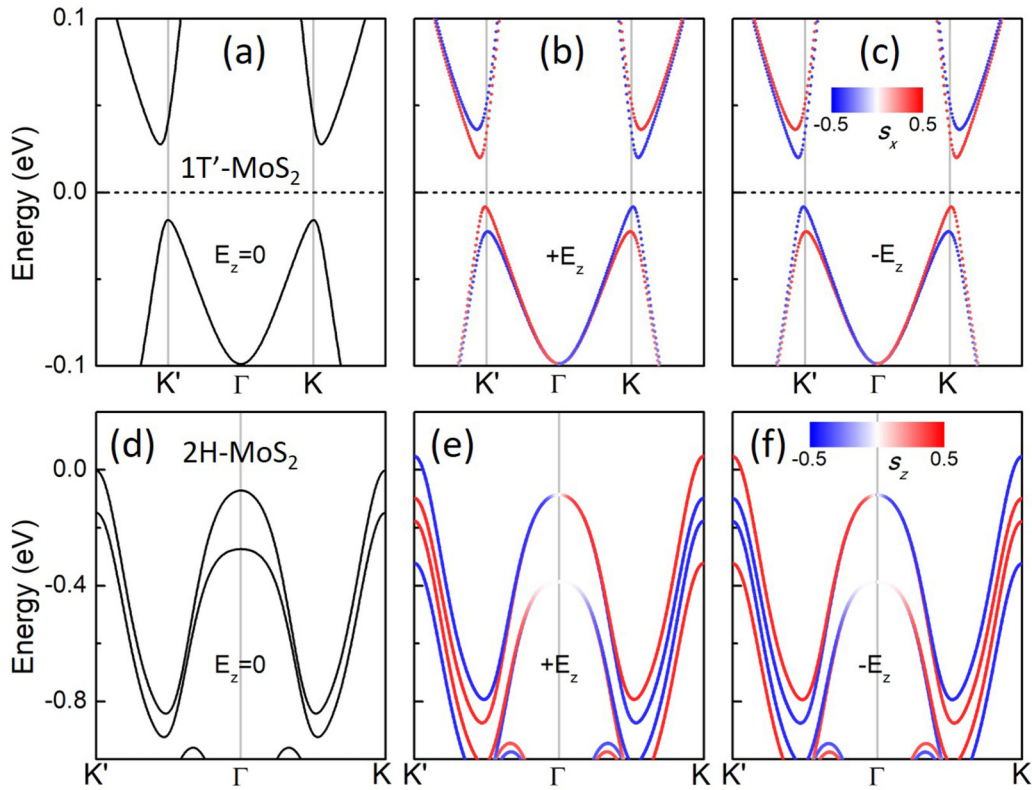


FIG. 5. Calculated band structure around the K and K' valleys for a $1T'$ -MoS₂ monolayer (a)–(c) and a $2H$ -MoS₂ bilayer (d)–(f) for $E_z = 5$ V/nm (b),(c) and $E_z = 1$ V/nm (e),(f). The color quantifies the expectation value of s_x (b),(c) and s_z (e),(f); the expectation values of the two other spin components being negligible.

practice. According to our calculations, for disorder providing realistic resistivity of stanene, the VSV ratio is maintained close to 100% (Supplemental Material Sec. 9 [43]). Given the above arguments, the experimental demonstration for the proposed valley spin valve is feasible.

In summary, we have proposed a valley spin valve, which relies on spin-valley locking induced by an applied electric field in 2D materials, such as germanene, stanene, $1T'$ -MX₂ ML, and $2H$ -MX₂ BL. The electric field breaks inversion symmetry in these materials, which in conjunction with spin-orbit coupling lifts the spin degeneracy and creates spin polarization opposite at the K and K' valleys. This property allows the valley spin polarization to be controlled by a gate voltage. We have demonstrated that placing two gates in series along the monolayer enables a valley spin polarizer and a valley spin analyzer to control the electric transport. The valley spin valve is ON or OFF depending on the relative valley

spin polarization of the polarizer and analyzer (i.e., being the same or opposite). Using quantum-transport calculations based on an adequate tight-binding model, we have predicted a giant VSV ratio of nearly 100% for both germanene- and stanene-based VSV devices. We argued that the proposed VSV is feasible to realize experimentally. We hope that our results will stimulate the experimentalists working in the fields of 2D materials and electronic devices to verify our predictions.

This research was supported by the National Science Foundation (NSF) through the E2CDA program (Grant No. ECCS-1740136) and the Semiconductor Research Corporation (SRC) through the nCORE program. Computations were performed at the University of Nebraska Holland Computing Center. The atomic structure figures were produced using the VESTA software [49].

- [1] X. Xu, W. Yao, D. Xiao, and T. F. Heinz, Spin and pseudospins in layered transition metal dichalcogenides, *Nat. Phys.* **10**, 343 (2014).
 [2] J. R. Schaibley, H. Yu, G. Clark, P. Rivera, J. S. Ross, K. L. Seyler, W. Yao, and X. Xu, Valleytronics in 2D materials, *Nat. Rev. Mater.* **1**, 16055 (2016).

- [3] I. Žutić, J. Fabian, and S. Das Sarma, Spintronics: Fundamentals and applications, *Rev. Mod. Phys.* **76**, 323 (2004).
 [4] S. Manzeli, D. Ovchinnikov, D. Pasquier, O. V. Yazyev, and A. Kis, 2D transition metal dichalcogenides, *Nat. Rev. Mater.* **2**, 17033 (2017).

- [5] T. Cao, G. Wang, W. Han, H. Ye, C. Zhu, J. Shi, Q. Niu, P. Tan, E. Wang, B. Liu, and J. Feng, Valley selective circular dichroism of monolayer molybdenum disulphide, *Nat. Commun.* **3**, 887 (2012).
- [6] H. Zeng, J. Dai, W. Yao, D. Xiao, and X. Cui, Valley-selective circular dichroism of monolayer molybdenum disulphide, *Nat. Nanotechnol.* **7**, 490 (2012).
- [7] K. F. Mak, K. L. McGill, J. Park, and P. L. McEuen, The valley Hall effect in MoS₂ transistors, *Science* **344**, 1489 (2014).
- [8] H. Yu, X. Cui, X. Xu, and W. Yao, Valley excitons in two dimensional semiconductors, *Natl. Sci. Rev.* **2**, 57 (2015).
- [9] D. Xiao, G. B. Liu, W. Feng, X. Xu, and W. Yao, Coupled Spin and Valley Physics in Monolayers of MoS₂ and Other Group-VI Dichalcogenides, *Phys. Rev. Lett.* **108**, 196802 (2012).
- [10] M. Gmitra and J. Fabian, Proximity Effects in Bilayer Graphene on Monolayer WSe₂: Field-Effect Spin Valley Locking, Spin-Orbit Valve, and Spin Transistor, *Phys. Rev. Lett.* **119**, 146401 (2017).
- [11] T. Zhou, J. Zhang, H. Jiang, I. Žutić, and Z. Yang, Giant spin-valley polarization and multiple Hall effect in functionalized bismuth monolayers, *npj Quantum Mater.* **3**, 39 (2018).
- [12] Z. R. Gong, G. B. Liu, H. Y. Yu, D. Xiao, X. D. Cui, X. D. Xu, and W. Yao, Magnetoelectric effects and valley controlled spin quantum gates in transition metal dichalcogenide bilayers, *Nat. Commun.* **4**, 2053 (2013).
- [13] G. Aivazian, Z. Gong, A. M. Jones, R.-L. Chu, J. Yan, D. G. Mandrus, C. Zhang, D. Zhang, W. Yao, and X. Xu, Magnetic control of valley pseudospin in monolayer WSe, *Nat. Phys.* **11**, 148 (2015).
- [14] D. MacNeill, C. Heikes, K. F. Mak, Z. Anderson, A. Kormányos, V. Zólyomi, J. Park, and D. C. Ralph, Breaking of Valley Degeneracy by Magnetic Field in Monolayer MoSe₂, *Phys. Rev. Lett.* **114**, 037401 (2015).
- [15] Y. C. Cheng, Q. Y. Zhang, and U. Schwingenschlögl, Valley polarization in magnetically doped single-layer transition-metal dichalcogenides, *Phys. Rev. B* **89**, 155429 (2014).
- [16] N. Singh and U. Schwingenschlögl, A route to permanent valley polarization in monolayer MoS₂, *Adv. Mater.* **29**, 1600970 (2017).
- [17] J. Qi, X. Li, Q. Niu, and J. Feng, Giant and tunable valley degeneracy splitting in MoTe₂, *Phys. Rev. B* **92**, 121403 (2015).
- [18] Q. Zhang, S. A. Yang, W. Mi, Y. Cheng, and U. Schwingenschlögl, Large spin-valley polarization in monolayer MoTe₂ on top of EuO(111), *Adv. Mater.* **28**, 959 (2016).
- [19] C. Zhao, T. Norden, P. Zhang, P. Zhao, Y. Cheng, F. Sun, J. P. Parry, P. Taheri, J. Wang, Y. Yang, T. Scrace, K. Kang, S. Yang, G.-x. Miao, R. Sabirianov, G. Kioseoglou, W. Huang, A. Petrou, and H. Zeng, Enhanced valley splitting in monolayer WSe₂ due to magnetic exchange field, *Nat. Nanotechnol.* **12**, 757 (2017).
- [20] L. Xu, M. Yang, L. Shen, J. Zhou, T. Zhu, and Y. P. Feng, Large valley splitting in monolayer WS₂ by proximity coupling to an insulating antiferromagnetic substrate, *Phys. Rev. B* **97**, 041405 (2018).
- [21] B. Scharf, G. Xu, A. Matos-Abiague, and I. Žutić, Magnetic Proximity Effects in Transition-Metal Dichalcogenides: Converting Excitons, *Phys. Rev. Lett.* **119**, 127403 (2017).
- [22] E. Y. Tsymlal, O. N. Mryasov, and P. R. LeClair, Spin-dependent tunnelling in magnetic tunnel junctions, *J. Phys.: Condens. Matter* **15**, R109 (2003).
- [23] L. L. Tao and J. Wang, Giant magnetoresistance and perfect spin filter effects in manganese phthalocyanine based molecular junctions, *Nanoscale* **9**, 12684 (2017).
- [24] A. Rycerz, J. Tworzydło, and C. W. J. Beenakker, Valley filter and valley valve in graphene, *Nat. Phys.* **3**, 172 (2007).
- [25] J. J. Wang, S. Liu, J. Wang, and J. F. Liu, Valley filter and valve effect by strong electrostatic potentials in graphene, *Sci. Rep.* **7**, 10236 (2017).
- [26] J. Nakabayashi, D. Yamamoto, and S. Kurihara, Band-Selective Filter in a Zigzag Graphene Nanoribbon, *Phys. Rev. Lett.* **102**, 066803 (2009).
- [27] D. Kochan, S. Irmer, and J. Fabian, Model spin-orbit coupling Hamiltonians for graphene systems, *Phys. Rev. B* **95**, 165415 (2017).
- [28] H. Yuan, M. S. Bahramy, K. Morimoto, S. Wu, K. Nomura, B. J. Yang, H. Shimotani, R. Suzuki, M. Toh, C. Kloc, X. Xu, R. Arita, N. Nagaosa, and Y. Iwasa, Zeeman-type spin splitting controlled by an electric field, *Nat. Phys.* **9**, 563 (2013).
- [29] Q. Liu, X. Zhang, H. Jin, K. Lam, J. Im, A. J. Freeman, and A. Zunger, Search and design of nonmagnetic centrosymmetric layered crystals with large local spin polarization, *Phys. Rev. B* **91**, 235204 (2015).
- [30] C. M. Acosta, A. Fazzio, and G. M. Dalpian, Zeeman-type spin splitting in nonmagnetic three-dimensional compounds, *npj Quantum Mater.* **4**, 41 (2019).
- [31] P. Vogt, P. De Padova, C. Quaresima, J. Avila, E. Frantzeskakis, M. C. Asensio, A. Resta, B. Ealet, and G. Le Lay, Silicene: Compelling Experimental Evidence for Graphene-Like Two-Dimensional Silicon, *Phys. Rev. Lett.* **108**, 155501 (2012).
- [32] C. C. Liu, W. Feng, and Y. Yao, Quantum Spin Hall Effect in Silicene and Two-Dimensional Germanium, *Phys. Rev. Lett.* **107**, 076802 (2011).
- [33] M. E. Dávila, L. Xian, S. Cahangirov, A. Rubio, and G. Le Lay, Germanene: A novel two-dimensional germanium allotrope akin to graphene and silicene, *New J. Phys.* **16**, 095002 (2014).
- [34] F. Zhu, W. Chen, Y. Xu, C. Gao, D. Guan, C. Liu, D. Qian, S. C. Zhang, and J. Jia, Epitaxial growth of two-dimensional stanene, *Nat. Mater.* **14**, 1020 (2015).
- [35] Y. Xu, B. Yan, H. J. Zhang, J. Wang, G. Xu, P. Tang, W. Duan, and S. C. Zhang, Large-Gap Quantum Spin Hall Insulators in Tin Films, *Phys. Rev. Lett.* **111**, 136804 (2013).
- [36] X. Qian, J. Liu, L. Fu, and J. Li, Quantum spin Hall effect in two-dimensional transition metal dichalcogenides, *Science* **346**, 1344 (2014).
- [37] C. C. Liu, H. Jiang, and Y. Yao, Low-energy effective Hamiltonian involving spin-orbit coupling in silicene and two-dimensional germanium and tin, *Phys. Rev. B* **84**, 195430 (2011).
- [38] M. Ezawa, Monolayer topological insulators: Silicene, germanene, and stanene, *J. Phys. Soc. Jpn.* **84**, 121003 (2015).
- [39] W. F. Tsai, C. Y. Huang, T. R. Chang, H. Lin, H. T. Jeng, and A. Bansil, Gated silicene as a tunable source of nearly 100% spin-polarized electrons, *Nat. Commun.* **4**, 1500 (2013).
- [40] S. Rachel and M. Ezawa, Giant magnetoresistance and perfect spin filter in silicene, germanene, and stanene, *Phys. Rev. B* **89**, 195303 (2014).

- [41] Kh. Shakouri, H. Simchi, M. Esmailzadeh, H. Mazidabadi, and F. M. Peeters, Tunable spin and charge transport in silicene nanoribbons, *Phys. Rev. B* **92**, 035413 (2015).
- [42] L. L. Tao, K. T. Cheung, L. Zhang, and J. Wang, All-electrical generation of spin-polarized currents in quantum spin Hall insulators, *Phys. Rev. B* **95**, 121407 (2017).
- [43] See Supplemental Material at <http://link.aps.org/supplemental/10.1103/PhysRevB.100.161110>, which includes Refs. [50–63], for the theoretical formalism, DFT computational details, electric field tunable band gap, gate width and separation distance dependences of the VSV effect, analysis of the scattering state, projected band structures for $1T'$ -MoS₂ and $2H$ -MoS₂, and effects of Rashba SOC and disorder.
- [44] M. Ezawa, Valley-Polarized Metals and Quantum Anomalous Hall Effect in Silicene, *Phys. Rev. Lett.* **109**, 055502 (2012).
- [45] Z. Y. Jia, Y. H. Song, X. B. Li, K. Ran, P. Lu, H. J. Zheng, X. Y. Zhu, Z. Q. Shi, J. Sun, J. Wen, D. Xing, and S. C. Li, Direct visualization of a two-dimensional topological insulator in the single-layer $1T'$ -WTe₂, *Phys. Rev. B* **96**, 041108 (2017).
- [46] J. Li, K. Wang, K. J. McFaul, Z. Zern, Y. F. Ren, K. Watanabe, T. Taniguchi, Z. H. Qiao, and J. Zhu, Gate-controlled topological conducting channels in bilayer graphene, *Nat. Nanotechnol.* **11**, 1060(2016).
- [47] J. Li, R. X. Zhang, Z. Yin, J. Zhang, K. Watanabe, T. Taniguchi, C. Liu, and J. Zhu, A valley valve and electron beam splitter, *Science* **362**, 1149 (2018).
- [48] Y. Zhang, T.-T. Tang, C. Girit, Z. Hao, M. C. Martin, A. Zettl, M. F. Crommie, Y. R. Shen, and F. Wang, Direct observation of a widely tunable bandgap in bilayer graphene, *Nature (London)* **459**, 820 (2009).
- [49] K. Momma and F. Izumi, VESTA 3 for three-dimensional visualization of crystal, volumetric and morphology data, *J. Appl. Crystallogr.* **44**, 1272 (2011).
- [50] S. Datta, *Electronic Transport in Mesoscopic Systems* (Cambridge University Press, Cambridge, England, 1997).
- [51] L. Zhang, Y. Xing, and J. Wang, First-principles investigation of transient dynamics of molecular devices, *Phys. Rev. B* **86**, 155438 (2012).
- [52] P. A. Khomyakov, G. Brocks, V. Karpan, M. Zwierzycki, and P. J. Kelly, Conductance calculations for quantum wires and interfaces: Mode matching and Green's functions, *Phys. Rev. B* **72**, 035450 (2005).
- [53] K. Xia, M. Zwierzycki, M. Talanana, P. J. Kelly, and G. E. W. Bauer, First-principles scattering matrices for spin transport, *Phys. Rev. B* **73**, 064420 (2006).
- [54] H. H. B. Sørensen, P. C. Hansen, D. E. Petersen, S. Skelboe, and K. Stokbro, Efficient wave-function matching approach for quantum transport calculations, *Phys. Rev. B* **79**, 205322 (2009).
- [55] S. Sanvito, C. J. Lambert, J. H. Jefferson, and A. M. Bratkovsky, Efficient wave-function matching approach for quantum transport calculations, *Phys. Rev. B* **59**, 11936 (1999).
- [56] I. Rungger and S. Sanvito, Algorithm for the construction of self-energies for electronic transport calculations based on singularity elimination and singular value decomposition, *Phys. Rev. B* **78**, 035407 (2008).
- [57] P. E. Blöchl, Projector augmented-wave method, *Phys. Rev. B* **50**, 17953 (1994).
- [58] G. Kresse and D. Joubert, From ultrasoft pseudopotentials to the projector augmented-wave method, *Phys. Rev. B* **59**, 1758 (1999).
- [59] G. Kresse and J. Furthmüller, Efficient iterative schemes for *ab initio* total-energy calculations using a plane-wave basis set, *Phys. Rev. B* **54**, 11169 (1996).
- [60] J. P. Perdew, K. Burke, and M. Ernzerhof, Generalized Gradient Approximation Made Simple, *Phys. Rev. Lett.* **77**, 3865 (1996).
- [61] S. Grimme, S. Ehrlich, and L. Goerigk, Effect of the damping function in dispersion corrected density functional theory, *J. Comput. Chem.* **32**, 1456 (2011).
- [62] M. Liao, Y. Zang, Z. Guan, H. Li, Y. Gong, K. Zhu, X.-P. Hu, D. Zhang, Y. Xu, Y.-Y. Wang, K. He, X.-C. Ma, S.-C. Zhang, and Q.-K. Xue, Superconductivity in few-layer stanene, *Nat. Phys.* **14**, 344 (2018).
- [63] J. Falson, Y. Xu, M. Liao, Y. Zang, K. Zhu, C. Wang, Z. Zhang, H. Liu, W. Duan, K. He, H. Liu, J. H. Smet, D. Zhang, and Q.-K. Xue, Type-II Ising pairing in few-layer stanene. [arXiv:1903.07627](https://arxiv.org/abs/1903.07627).